# Phase controlled epitaxy of wurtzite ZnS thin films by metal organic chemical vapor deposition

Hassan Melhem, Geraldine Hallais, Gaelle Amiri, Gilles Patriarche, Nathaniel Findling, Theo van den Berg, Hafssa Ameziane, Charles Renard, Vincent Sallet, Laetitia Vincent

Thin Solid Films 812 (2025) 140609

Contents lists available at ScienceDirect

Thin Solid Films

journal homepage: www.elsevier.com/locate/tsf

# Phase controlled epitaxy of wurtzite ZnS thin films by metal organic chemical vapor deposition

Hassan Melhem [a], Geraldine Hallais [a], Gaelle Amiri [b], Gilles Patriarche [a], Nathaniel Findling [a], Theo Van den Berg [a], Hafssa Ameziane [a], Charles Renard [a], Vincent Sallet [b], Laetitia Vincent [a,*]

[a] Centre de Nanosciences et Nanotechnologies, Université Paris Saclay, CNRS, 91120 Palaiseau, France
[b] Groupe d'étude de la matière condensée (GEMAC), CNRS, Université de Versailles St Quentin en Yvelines, Université Paris-Saclay, 78035 Versailles Cedex, France

ARTICLE INFO

*Keywords:*
Epitaxy
Polytypism
Metal organic chemical vapor deposition
M-plane
II-VI semiconductor
X-ray photoelectron spectroscopy
Transmission electron microscopy

SUMMARY

In many semiconductors, metastable polytype phases are attractive to tune physical properties. Owing to a non-centrosymmetric structure, ZnS with a wurtzite (WZ) phase would exhibit additional piezoelectric properties, optical non-linearity as well as Rashba effect. Because bulk single crystalline ZnS-WZ is not commercially available in useful sizes and attractive prices, large area thin films with controlled crystalline phase are required. We report the synthesis of ZnS films deposited on m-plane CdS substrates as a proof of concept of the replication of the WZ stacking on non-polar surfaces. First, a chemical mechanical polishing is required for the substrate preparation. ZnS layers are subsequently grown using metal organic chemical vapor deposition. The results show a strong impact of the growth temperature on the CdS substrate surface that is highly detrimental on the crystalline quality of the layer. However, the m-plane ZnS layers grown at 360 °C have WZ structure with a perfect epitaxial orientation relationship with the CdS-WZ substrate. The hexagonality in ZnS-WZ is about 90 %. Strain relaxation occurs through the formation of misfit dislocations at the interface forming basal and prismatic stacking faults on {11–20} planes. Additional pyramidal planar defects are evidenced. With the optimisation of a buffer layer or a more suitable substrate, this ZnS-WZ layers may find various applications not limited to optics such as piezoelectricity or spintronics. Additionally, they may be used as a platform for the growth of other materials with the envisioned WZ structure.

## 1. Introduction

Zinc sulfide (ZnS), a versatile compound, finds applications in various fields of optics and optoelectronics. To give an emblematic example, ZnS is the old luminescent material employed for decades in cathode-ray tubes. Sintered ceramics of ZnS are also largely used as transmitting optical components in thermal imaging, owing to the high transmission in the visible and mid-infrared range from 0.4 to 14 μm. For such applications, polycrystalline ZnS are currently commercially available and are synthesized through different methods, including precipitation, solvothermal and chemical vapor deposition (CVD) processes, with adequate control of impurities (see for instance reviews in [1,2]). The grain size is sensitive to the process temperature and any possible annealing. Also, the as-grown polycrystalline CVD ZnS has to be further processed by hot isostatic pressing to get acceptable IR transmission properties. Because absorption and scattering are highly sensitive to defects and grain boundaries, single crystals of ZnS often exhibit superior optical and electronic properties compared to polycrystalline forms, making them desirable for other applications such as phosphor materials, UV-detectors and electroluminescent diodes.

Yet, ZnS has a higher tendency to disordered stacking and polytypism compared to CdS. 194 polytypes are referenced for ZnS [1,3,4]. Some polytypes can be stabilized by the presence of vacancies or impurities [5]. Natural crystals with a pure crystal phase can be found but they are always highly contaminated with Mn or Fe that is a luminescence killer. Among the various polytypes, zinc blende (ZB) and wurtzite (WZ) are the two thermodynamically metastable phases [6–8]. The stability of both phases is primarily dependent on the temperature [8,9]. The synthesis at low temperature favours ZB structure and the transition temperature is above 1020 °C [10–13].

* Corresponding author.
*E-mail address:* laetitia.vincent@c2n.upsaclay.fr (L. Vincent).

https://doi.org/10.1016/j.tsf.2025.140609
Received 6 August 2024; Received in revised form 9 January 2025; Accepted 17 January 2025
Available online 25 January 2025

Bulk ZnS are commonly synthesized using the Bridgman method at high pressure. Melt-grown ZnS are initially WZ at high temperature but transform very quickly in ZB with a significant defect density and a large amount of impurities. The WZ structure can however be stabilized with some dopants (Al, Cu, Mn) by rapid quenching [12] although having a large fraction of stacking faults or even a mixture of cubic and polytypes. Crystallization from vapor has advantages over melt growth to be carried out at lower temperatures. ZnS-ZB crystals have been grown by chemical vapor transport using HCl, $NH_4Cl$ or $I_2$ for transport but highly doped with iodine in the latter case [14,15]. Physical vapor transport (sublimation followed by condensation) showed to favour the formation of WZ structure but the size of pure crystal phase is very small. Whatever the synthesis method and conditions, it is very difficult to obtain chemically pure ZnS single crystal with a controlled crystal phase [3].

For many applications a chemically pure and single crystal phase is desirable. Controlling the polytype stacking is an efficient way to modify physical properties of materials. In particular, ZnS-WZ has a slightly larger band gap value than those of ZnS-ZB (respectively 3.91 eV and 3.61 eV). Belonging to the non-centrosymmetric $P6_3/mmc$ space group, the wurtzite structure is anisotropic. Consequently, ZnS-WZ may present additional exiting properties such as piezoelectric effect, optical non-linearity and Rashba effect which should be enhanced in thin films or nanostructures.

Because bulk ZnS-WZ is not available with good quality and low impurity, epitaxy of thin films is of particular interest to promote the growth of this polytype. Extensive efforts have been focused on improving the quality of epitaxial films of ZnS by vapor phase epitaxy (VPE) including metal organic chemical vapor deposition (MOCVD) [16–25] and molecular beam epitaxy (MBE) [26–34], as well as by atomic layer epitaxy (ALE) [35,36] and pulsed laser deposition [37,38]. Most of the reported growth were done on GaAs, GaP and Si substrates with which ZnS is fairly lattice matched (lattice mismatch is respectively of 4 %, 0.7 % and 0.2 %). However, the synthesis of high quality of epitaxial ZnS thin films with the desired WZ phase has never been achieved in a controlled way since the lowest energy stable phase is the ZB structure. To control the growth of metastable polytype, the choice of the substrate orientation is determinant. For instance, the growth of GaN on (001)-oriented substrates (either GaAs or SiC) favours the metastable ZB structure in defiance to the lowest energy WZ phase and in agreement with the minimum lattice mismatch criterion [39,40]. Our approach is to use a hexagonal template with non-basal surface orientations to force the arrangement of atoms to be replicated. Very few attempts were made to grow ZnS on non-polar hexagonal substrates. Only, two papers mentioned without any details the growth on a-plane sapphire substrates [24,41]. Despite a lattice mismatch over 20 %, the results proved the possible epitaxial growth of the WZ structure at low temperature with a specific orientation relationship with the substrate although the film consists of a mixture of WZ and twinned ZB. More recently, Okita et al. [42] reported the growth of a (1–100) ZnS-WZ layer epitaxially oriented on a m-plane (1–100) ZnO buffer deposited on (1–100) sapphire substrate. The intermediate ZnO layer aimed at reducing the lattice mismatch between the ZnS layer and the sapphire substrate, providing beneficial advantage for the epitaxy. However, the growth of ZnO on m-plane likely causes some stacking faults on the (0001) planes that may expand in the ZnS layer. On a completely relaxed ZnO buffer, the lattice mismatch of ZnS on m-plane is of 18 % along a-axis and 20 % along c-axis, still introducing high in-plane compression stress in the layer. Our present purpose is to use a substrate with lower lattice mismatch to demonstrate the feasibility of epitaxial growth of the metastable ZnS-WZ on m-plane surfaces. Contrarily to ZnS, the WZ structure is the lowest energy phase for CdS [7] with higher stacking fault energy and it is commercially available as a synthetic single crystal with m-plane surface. On CdS-WZ, ZnS is expected to be of 7.63 % and 6.83 % in tension along a and c axis respectively [43,44]. Additionally, from calculations reported in literature, it is considered that the surface energy of ZnS m-plane is slightly lower than that of CdS m-plane, with respectively, 0.51 $J/m^2$ and 0.6 $J/m^2$. This leads us to assume a Stranski-Krastanov growth [45,46].

Here, we use metal organic chemical vapor deposition (MOCVD) process to grow ZnS on a m-plane CdS substrate. This process at medium temperature allows epitaxy over large areas and gives advantage of high chemical purity and control of intentional doping. We set up a chemico-mechanical procedure for surface preparation of the CdS surface prior to MOCVD growth. We evidence the detrimental impact of temperature on the interface and we report epitaxy of single crystal layer of ZnS-WZ on m-plane CdS-WZ.

## 2. Material and methods

CdS-WZ substrates with the m-plane surfaces were obtained from Biotain and Surfacenet companies. The supplied substrates do not have intended off-cut angle.

ZnS thin films are grown in a vertical MOCVD reactor operating at atmospheric pressure. The MOCVD equipment and the growth regimes of ZnS-ZB on (001)-GaAs has been described in [47]. The reactor walls, made of quartz, are water cooled at 20 °C to limit the parasitic reactions on hot surfaces. The substrate holder, including a thermocouple positioned inside, is made of SiC-coated graphite and can be heated up to 1000 °C by RF induction. High purity diethylzinc (DEZn) and ditertiarybutylsulfide (DTBS), stored in stainless steel bubblers, are used as the zinc and sulfur metalorganic sources. Their thermal decompositions are suitable for growth at low temperatures starting from approximately 300 °C [48–50]. Inside the bubbler, when maintained at 17 °C, the vapor pressure is estimated to be 1356 Pa and 518 Pa for DEZn and DTBS, respectively. Hydrogen is the carrier gas.

In the present work, to favour the layer-by-layer growth mode on the m-plane CdS-WZ, the growth was carried in sulfur-rich conditions with a VI/II ratio of $R_{S/Zn} = 2$ using very low precursor partial pressures and hence low growth rates. Before introducing the metalorganic flows into the reactor, the substrate was heated to the growth temperature under hydrogen with DTBS supply (corresponding to a partial pressure of 8 Pa), with temperature ramp of 1 °C/s. The sulfur atmosphere is believed to reduce vaporization of CdS surface and avoid its degradation [51].

ZnS layers were first deposited at 520 °C to favour the mass transport regime and enhance surface diffusion. However, anisotropic substrate desorption and interdiffusion was observed, as described in the result section, and consequently the growth temperature was reduced to 360 °C. Details of the growth conditions are summarized in the Table 1.

X-ray photoelectron spectroscopy (XPS) measurements were carried out in a XPS ScientaOmicron equipped with a non-monochromatized $Al_\alpha$ source. The pressure in the analysis chamber is below $9.33 \times 10^{-7}$ Pa. The High-Resolution X-ray Photoelectron Spectroscopy (HR-XPS) spectra were acquired with a pass energy of 20 eV with an energy step size of 0.05 eV. The peak fitting was performed using Casa XPS software with a relative sensitivity factor given in the software database. Relative atomic concentrations were determined by analyzing the intensities of major photoelectron spectral lines (integrated peak areas) following the subtraction of a Tougaard background. The binding energies were calibrated by taking carbon C1s peak (284.8 eV) as a reference.

Atomic force microscopy (AFM) data were acquired under ambient conditions using a BRUKER Icon AFM operating in tapping mode with Veeco Silicon tip. The roughness values were assessed by standard RMS (Root Mean Square) measurements.

Cross-section lamellae prepared with Focused ion beam (FIB) were observed by scanning transmission electron microscopy (STEM) using a FEI ThermoFisher/STEM Titan Themis 200 equipped with an extreme-brightness field emission gun (X-FEG) operating at 200 keV. This instrument offers a range of characterization tools such as energy dispersive spectroscopy (EDS), bright field and high angle annular dark field (HAADF) STEM detectors.

X-ray diffraction (XRD) measurements were performed using an XPERT PRO MRD Panalytical diffractometer with a Bartels Ge 220

**Table 1**
Growth parameters for the samples described in the paper.

| Sample ref | Tg | $P_{Zn}$ (Pa) | $P_S$ (Pa) | Duration (min) | Deposited thickness (nm) | Comments |
|---|---|---|---|---|---|---|
| S1 (MV1175) | 520 °C | 4 | 8 | 30 | 220 ± 18 | CdS annealing during 5 min at 580 °C under DTBS before introduction of DEZn |
| S2 (MV1242) | 360 °C | 2 | 4 | 8 | 41.6 ± 2 | Growth temperature of 360 °C reached in 5 min under DTBS flow, no annealing before introduction of DEZn |
| S3 (MV1243) | 360 °C | 2 | 4 | 6 | 28.6 ± 1.5 | |
| S4 (MV1244) | 360 °C | 2 | 4 | 4.5 | 19.4 ± 1.2 | |
| S5 (MV1245) | 360 °C | 2 | 4 | 3 | 10 ± 0.9 | |
| S6 (MV1332) | 360 °C | 7.82 | 15.96 | 30 | 545 ± 25 | |

monochromator under ambient conditions, utilizing a copper Kα radiation (λ = 1.5406 Å). The XRD scan was conducted in a parallel beam mode with a beam size of 5 mm x 2 mm, following a rocking curve path. The time per scan was approximately 50 min with a step size of 1 s, and the alignment was performed on the CdS substrate.

## 3. Results and discussion

### 3.1. Surface preparation of CdS substrates

The structural quality of an epitaxial layer primarily relies on an ideal smooth and perfectly clean substrate surface. Thus, the first challenge is to set an efficient and reliable substrate to get rid of any roughness or surface contaminant that may cause the formation of defects at the interface. The as received m-plane CdS-WZ substrates were cleaned with acetone and ethanol. The measured root mean square was about 0.45 nm ± 0.2 nm. XPS analyses are displayed in Fig. 1. The measurements on as received samples highlight the presence of oxygen and carbon in addition to the cadmium and sulfur elements of the substrate. Traces of Cl contamination were also found on the surface most likely brought by the polishing performed by the supplier. The O1 s peak profile (Fig. 1a) can be decomposed into three components located at 529.6 eV, 531.7 eV and 533.4 eV corresponding respectively to the O—Cd bond, the indissociable Cd—OH/C—O—H, O—C—O, C = O bonds and a pure organic O—C = O bond [52–54]. The C 1s spectrum (Fig. 1b) confirms the presence of organic contamination, according to its deconvolution into 4 component peaks: the component peak at 288.4 eV can be assigned to purely organic bonds C = O and O—C-O, the component peak at 285.9 eV is assigned to the C—OH bond, the component peak at 284.8 eV is assigned to C sp2/sp3 and finally the component peak at lower energy 282.3 eV corresponds to the C—Cd links with low intensity.

For the Cd (Fig. 1c), the 3d core-level spectrum decomposition showed the presence of the characteristic doublet with the 3d5/2 at 405.1 eV and the 3d3/2 at 411.8 eV corresponding at Cd—S bonds. An additional doublet was found at a lower binding energy (3d5/2 at 404.8 eV and 3d3/2 at 411.5 eV), which is related to Cd—Cd and/or Cd—O bonds. A third doublet at higher energy (3d5/2 at 406.4 eV) correspond at a bonding with the Cl contamination. The S 2p spectrum, displayed in Fig. A1 in appendix A, does not evidence sulfur-oxygen bonds; S is only linked to Cd (S 2p3/2 at 161.4 eV and S 2p1/2 at 162.5 eV as in ref [55, 56]). It is also important to note that the surface is sulphur deficient compared to Cd (see quantification in Fig. 1d).

For many substrates, thermally stimulated desorption may be applied to desorb the O and C contaminants. However, II-VI compounds are known to dissociate and evaporate above 470 °C under vacuum [57]. The vaporization of CdS is known to be congruent by desorption of $S_2$ and Cd atoms. The vaporization rate of CdS single crystal is higher on m-plane compared to c-plane [58] and it was reported that the non-polar surfaces of CdS are not stable under vaporization [59,60]. Babasian and Givargizov [51,61] described the formation of "negative whiskers" by evaporation of ZnS and CdS under hydrogen accounted for a kinetic regime of evaporation at low temperature (<830 °C). The negative whiskers were formed on the metal-terminated polar c-plane and can be enhanced by the presence of metal liquid layer such as gold. They had a hexagonal shape with six large spikes and additional numerous narrow grooves characteristic of CdS (see Fig. 5 in ref [61]). This effect was ascribed to a solid-liquid-vapor mechanism related to a catalytic effect of vaporization.

In this study, thermal desorption has been carried out on as-received m-plane CdS subtrates, under ultra-high vacuum as well as under atmospheric pressure with $H_2$+DTBS flow. The desorption under DTBS was achieved during 10 min at 520 °C. It appears that the roughness of the surface was degraded. After annealing under DTBS, the RMS is 3 times higher of 1.78 ± 0.2 nm. More importantly, we observe the formation of a large density of thin and deep vertical grooves elongated along the c-axis (Fig. 2 and Fig. A4 in appendix) leading to a highly damaged surface unsuitable for further epitaxy at high temperature. Lowering the annealing temperature would help in reducing the surface damaging, however XPS in-situ analyses performed after thermal annealing under vacuum reveal only partial surface deoxidation at 400 °C and 500 °C and a larger deficiency in sulfur (Fig. 1d). Carbon is still present but may also increase during annealing in our chamber due to cross contamination.

Thus, for deoxidation and decontamination, thermal annealing was replaced by a chemical mechanical polishing (CMP) using a final step with a diluted bromine methanol ($Br_2$_MeOH) solution. Alcoholic bromine is the most widely used chemical etchant of II-VI compounds [62] although the polished surface of CdS was shown less smooth than for ZnS and CdSe [63]. Typically, a classical etching of CdS produces an "orange peel texture" on the surface depending on bromine concentration. To avoid this, we performed a final polishing with a soft polishing cloth and a highly diluted solution of bromine-methanol with a concentration of 0.01 %. After this CMP process, the XPS survey spectrum reveals the disappearance of the Cl contamination but the presence of Br contamination at about 1.5 at.% evidenced by the presence of the doublet Br 3p3/2 and Br 3p1/2 (see Appendix Fig. A2). In Fig. 1c, the deconvolution of the peak Cd 3d5/2 reveals an additional peak at 406.1 eV characteristic of the Cd—Br bonds [64]. Given the highly volatile nature of bromine, annealing at low temperature enables to get rid of bromine without damaging the surface quality. HR-XPS Cd $3d_{5/2}$ spectrum obtained after CMP and successive annealing at 350 °C during 20 min under ultra-high vacuum has therefore a unique component at 405.1 eV corresponding to Cd—S binding alone. In addition, the CMP remarkably removes the O—Cd bonds (with the disappearance of the peak at 529.6 eV (Fig. 1a)) and C—Cd (with the disappearance of the peak at 282.3 eV (Fig. 1b)) present on the surface of a substrate as received.

The histogram in Fig. 1d summaries the HR-XPS quantifications obtained on an as-received sample and after the successive surface

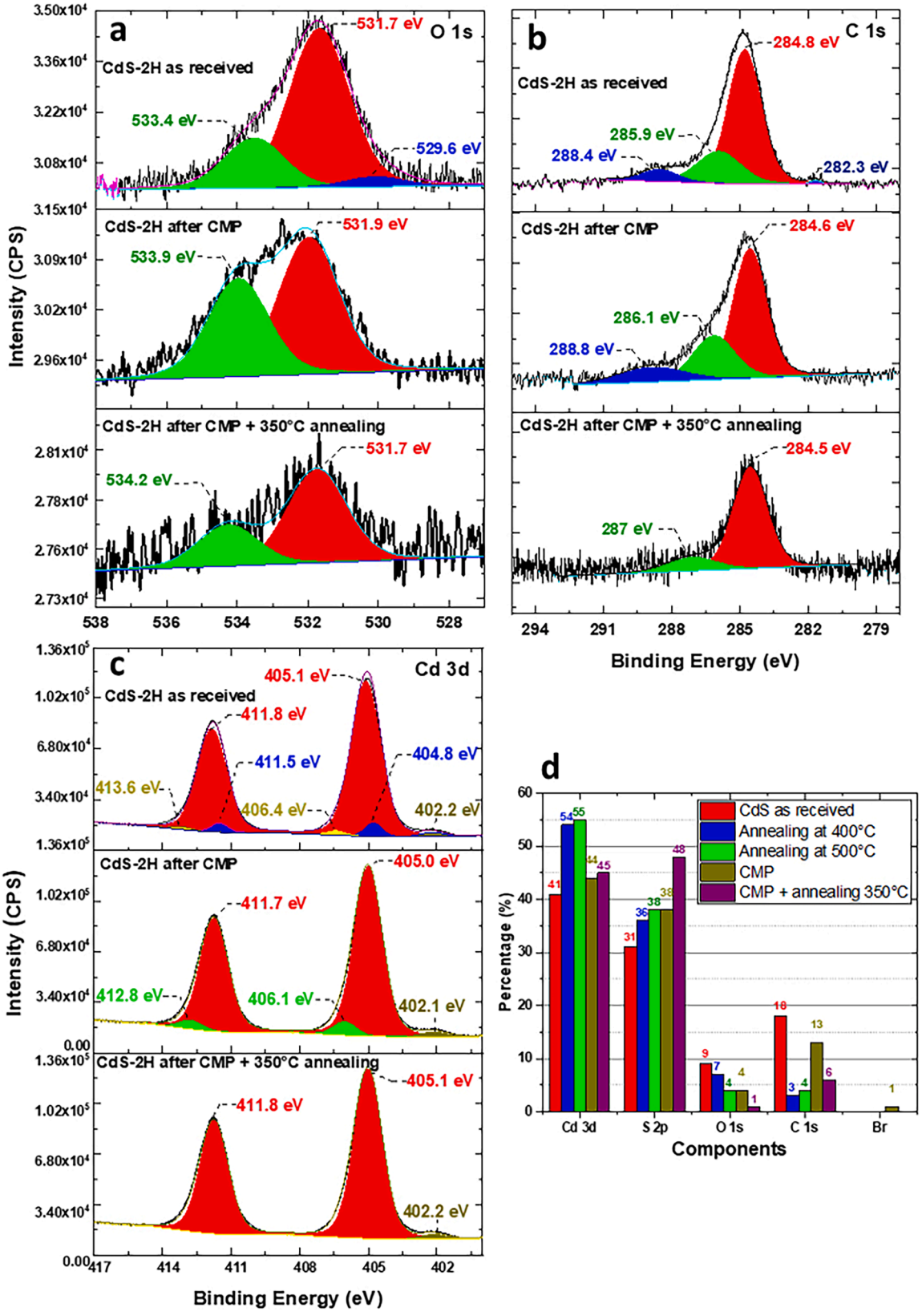


**Fig. 1.** High-resolution XPS spectra of the O 1 s, C 1 s, and Cd 3d core level respectively in (a), (b), and (c), comparing an as-received CdS sample and the same sample after CMP polishing with Br:$CH_3OH$ and after annealing. The fittings were performed using Casa XPS software. (d) Chemical quantifications of CdS surface depending on the various surface treatments.

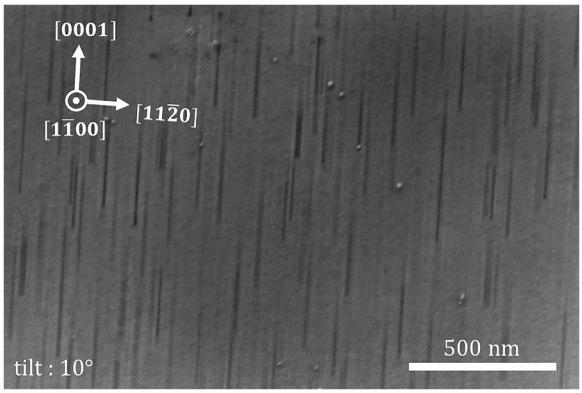


**Fig. 2.** SEM micrograph of the CdS m-plane surface showing the formation of elongated grooves after thermal desorption at 520 °C under DTBs atmosphere during 10 min The image was recorded on a 10°tilted plan view.

preparation steps on the same sample. On as-received sample, the oxide and carbon contaminants are of about 9 and 18 at.% respectively. Although annealing at 400 °C or 500 °C under UHV during 15 min enables a reduction of contaminants, a higher sulfur deficiency is noticed, which is assumed to be related to CdS vaporization and grooves formation. The sequential process of CMP and annealing at 350 °C enables us to remove bromine (polishing contamination) and to significantly reduce oxygen to around 1 %. Although the carbon contamination is still at around 6 %, it was considered not detrimental for the growth, but this need to be improved in the future. Besides, we note a recovered stoichiometry Cd/S after the overall process. And importantly, the thermal annealing at this low temperature does not create grooves on the surface. According to AFM measurements, the surface after CMP followed by annealing at 350 °C showed no signs of groove formation and displayed a roughness similar to the untreated sample. All RMS measurements after each process step are reported in Table 2 (additional information are reported in appendix in Fig. A3).

### 3.2. Deposited layer at 520 °C

Fig. 3a shows a top view scanning electron microscopy (SEM) micrograph of the ZnS layers grown at 520 °C (Table 1 - sample S1 220 nm). The growth is planar but the layer exhibits a rough surface with triangular prismatic structures aligned along the c axis. Lamellae were cut with focused ion beam (FIB) for TEM observations along <0001> and ⟨11–20⟩ zone axes (ZA). The ⟨0001⟩ ZA micrograph in Fig. 4a clearly reveals a sawtooth shape related to the prismatic structure observed in Fig. 3a. Nonetheless, the selective area diffraction pattern (SAED) shown in insert attest to the wurtzite crystal phase of the ZnS layer. The formed facets on the surface could not be indexed to any low-index plane of the hexagonal structure, neither a, m or r-plane.

In Fig. 3a, it is also shown the formation of very straight microcracks on a-planes. These microcracks are likely caused by stress relaxation either due to the difference in thermal expansion coefficients (TEC) between ZnS and CdS or excessive tensile stress in the ZnS film during cooling.

More importantly, cross sections in Fig. 4b and c clearly unveil a highly degraded CdS/ZnS interface. Along the ⟨0001⟩ ZA, large ellipsoidal cavities are observed with bright contrast using bright field imaging. These cavities appear as holes of about 10 nm long, below the interface. They correspond to the elongated grooves aligned along ⟨0001⟩ (described in Fig. 2 and appendix Fig. A4). It is likely that during the temperature rise before growth at 520 °C, grooves were rapidly formed due to desorption and they were later buried rather than filled by ZnS leading to the observed cavities. Although the deposited ZnS layer is continuous, the grooves formed in CdS, at high temperature, may induce the formation of defects or even cubic segments as explained in Section 4.

Along the ⟨11–20⟩ ZA, the cavities are visible with HAADF contrast as dark tunnels below the interface (Fig. 4d and e). The micrograph, in Fig. 4e shows also additional dark blurred contrasts perpendicular to the interface. This Z-contrast suggests an important chemical inhomogeneity. EDS map in Fig. 4f evidences an important diffusion of Zn in CdS on more than 30 nm. The non-homogeneous distribution of Zn in the Cd could be also related to the formation of those cavities.

Although the deposited ZnS layer is continuous, the formation of grooves in CdS is detrimental for the crystal quality as will explained in Section 4 and in Fig. A5 from appendix A lower growth temperature was used to get rid of these grooves.

**Table 2**
Measured RMS after successive step of surface preparation process.

| Sample | RMS (Rq) (nm) |
|---|---|
| CdS as-received | 0.46 ± 0.22 (S1) |
| After CMP | 0.40 ± 0.07 (S1) |
| After annealing at 360 °C under UHV | 0.377 ± 0.035 |
| After annealing at 520 °C under UHV | 0.863 ± 0.196 |

### 3.3. Deposited layer at 360 °C

At 360 °C, the microcracks are still present as well as the elongated prismatic structures although less prominent (see Fig. 3b of sample S2 and additional Fig. A5). From SEM micrograph the roughness appears lower but it could be associated to a lower deposited thickness (41.6 nm) and a reduced growth time, although the temperature may have an impact. This results in a less defined faceting compared with sample S1.

Fig. 5 shows the TEM micrographs of samples grown at 360 °C along both ⟨0001⟩ and ⟨11–20⟩ ZA. Comparing Figs. 4 and 5, shows that the growth temperature highly impacts the stability of the substrate surface. Lowering the process temperature to 360 °C enables to avoid the cavity formation (Fig. 5d) and reduces the Zn diffusion in the CdS substrate, as shown in Fig. 5e. However, the STEM HAADF bright contrast on the micrographs in Fig. 5c and d gives hints of local enrichment in Cd which is likely associated to enhanced diffusion of Zn forming Zn enriched channels below the surface.

### 3.4. Structural characterisations of epitaxial ZnS-WZ layers

The layers grown at 360 °C were characterized by XRD ω−2θ scans shown in Fig. 6. Besides the diffraction peaks from the CdS-WZ substrate, the XRD patterns show three peaks attributed to {1–100} planes of ZnS-WZ (JPCDS, No 36–1450). This indicates the epitaxy of a monocrystalline ZnS-WZ thin film on CdS-WZ with a single out of plane orientation. Based on lattice spacing measured in XRD patterns, the a and c calculated lattice parameters are 3.797 Å and 6.216 Å respectively, in good agreement with the reported values of 3.821 Å and 6.257 Å [43], supporting a complete relaxation of the deposited wurtzite layer. The peak intensity related to ZnS-WZ increases with the film thickness. The full width at half maximum (FWHM) of the (1–100) reflection of ZnS-WZ is around 0.82° for all samples (see appendix Fig. A6), that should be compared to the FWHM of 0.063° for the CdS-WZ substrate.

In Figs. 4 and 5, SAED patterns on cross sections along [0001] and [11–20] ZA show a highly ordered layer ZnS-WZ layer on CdS-WZ with the orientation relationship $[11–20]_{ZnS}$// $[11–20]_{CdS}$, $(1–100)_{ZnS}$// $(1–100)_{CdS}$ and $(0001)_{ZnS}$//$(0001)_{CdS}$. With SAED, interplanar distance of ZnS (10–10) planes was measured at 3.31 Å and those of (11–20) planes at 1.91 Å.

In Fig. 7, the high-resolution HAADF STEM micrographs along the [11–20] ZA shows the ZnS/CdS interface and the alignment of basal planes. This specific ZA enables us to discriminate between the cubic and hexagonal stacking on the basal planes. In Fig. 7, basal stacking faults

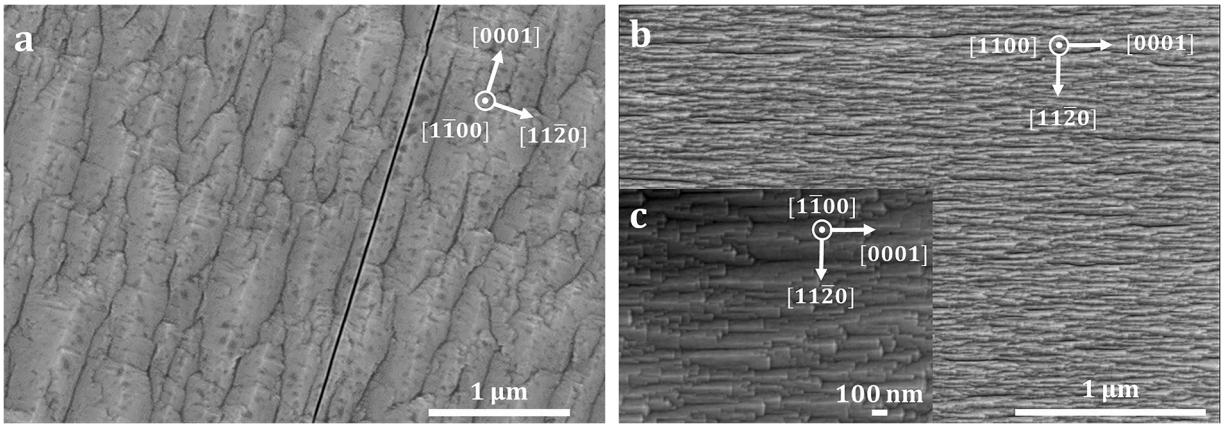


**Fig. 3.** SEM micrographs exhibiting the surface morphology of the ZnS layer on CdS-2H substrate, grown at (a) 520 °C (sample S1), and (b) 360 °C (sample S2). Prismatic structures are aligned along the [0001] direction.

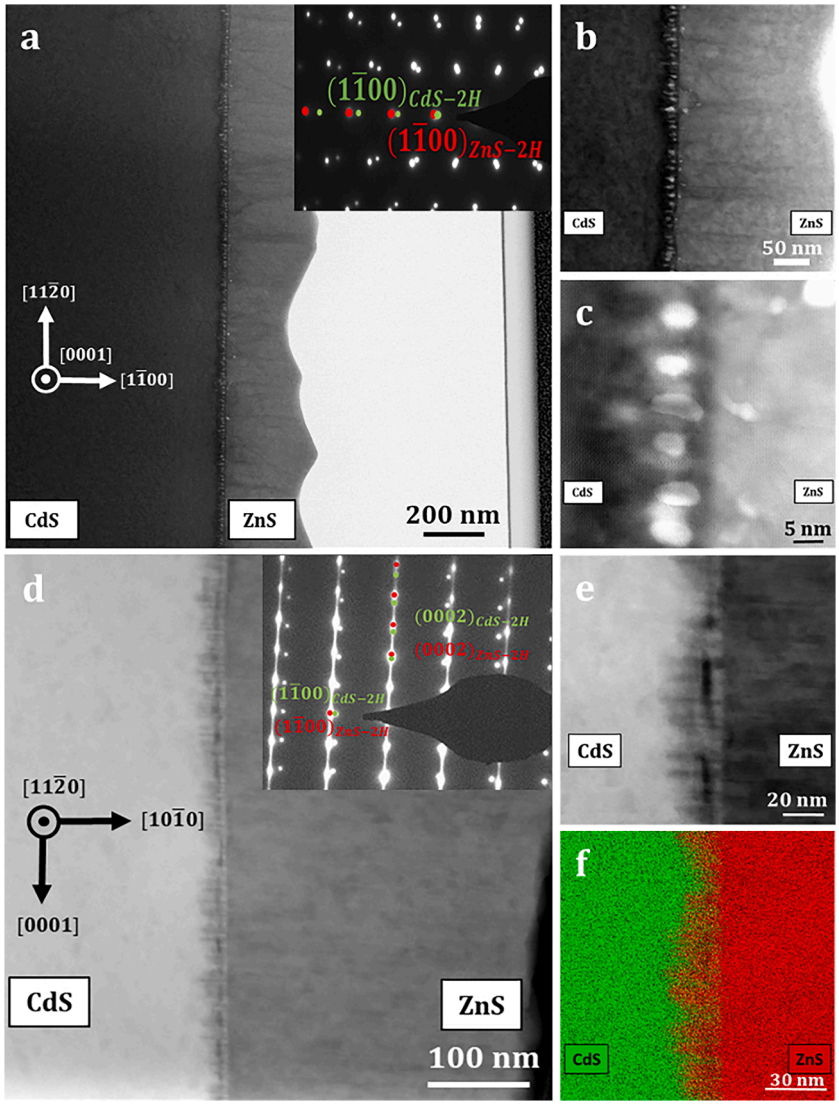


**Fig. 4.** Bright field (a, b and c) and HAADF (d and e) STEM micrographs associated with EDS mapping (f) of a cross-sectional ZnS layer grown on m-plane CdS at 520 °C. Micrographs are taken respectively along [0001] ZA (a-c) and [11–20] ZA (d-f). In a) and d) for enlarged views, the SAED patterns given in inset evidence the hexagonal 2H stacking of ZnS-WZ and the epitaxial orientation relationship with the CdS-WZ substrate. In b and c) bright field images along [0001] ZA show a zoom-in of the interface and exhibit the formation of large cavities below the CdS substrate. e) Shows a HAADF zoom-in of the interface along the perpendicular [11–20] ZA. The cavities, visible as dark elongated contrasts, ressemble tunnels along [0001]. In f) the EDS mapping associated to e) shows the diffusion of Zn.

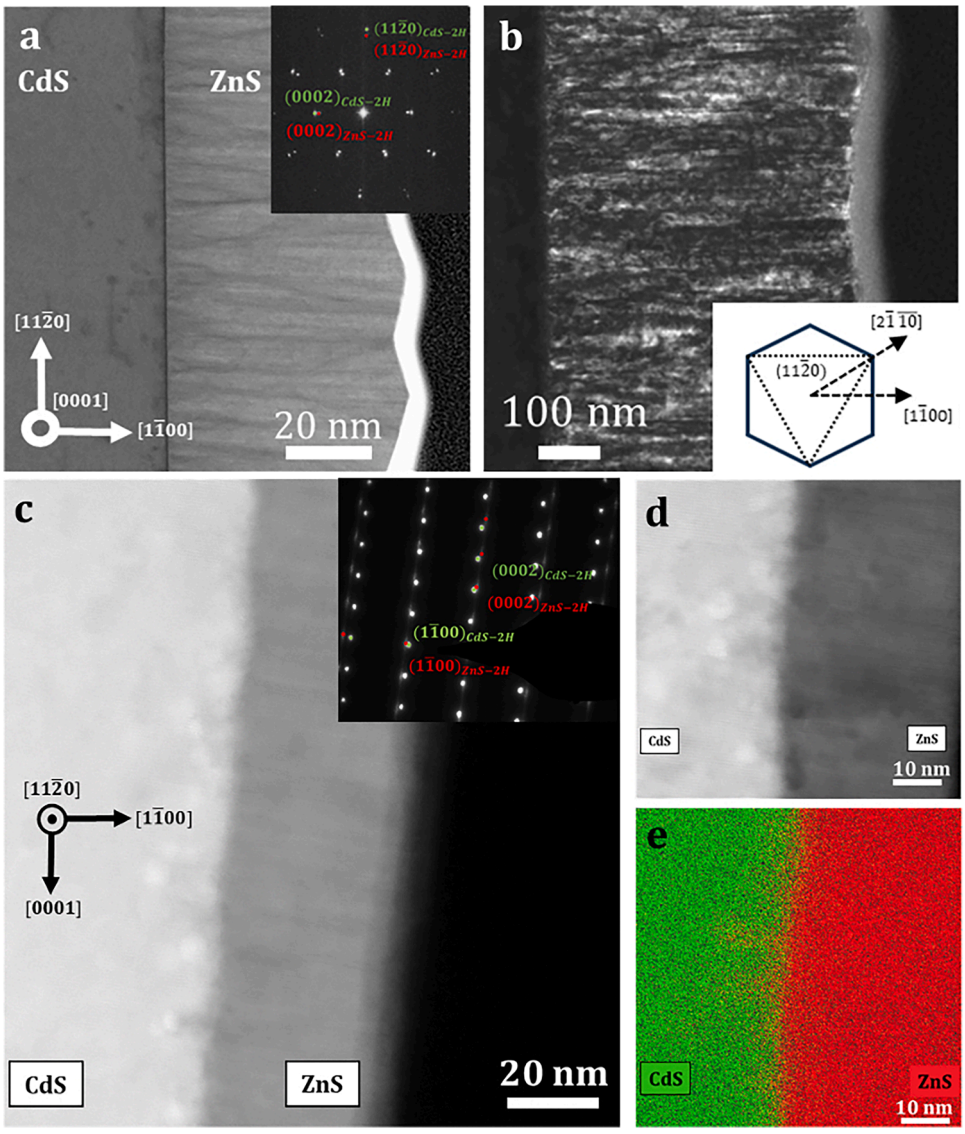


**Fig. 5.** Bright/dark-field field (a and b) and HAADF (c and e) STEM micrographs associated with EDS mapping (d) of a cross-sectional ZnS layer grown on m-plane CdS at 360 °C (samples S2 and S6). Micrographs are taken respectively along [0001] ZA (a-b) and [11–20] ZA (c-e). In a) and d) for enlarged views, the FFT or SAED patterns are given in inset and evidence the WZ stacking of ZnS and the epitaxial orientation relationship with the CdS-WZ substrate. In b) dark field is acquired near [0001] ZA with a Bragg reflection of (11–20) to evidence the prismatic stacking faults that appear edge on. The inset gives a schematic of the prismatic planes projected on basal plane along the [0001] ZA and provide the main directions for the hexagonal structure. Solid lines show the {1–100} prismatic planes and dashed lines show the {11–20} prismatic planes. The (11–20) planes are horizontal as in the micrograph b). Thus bright contrasts in the micrograph indicate stacking faults on (11–20) planes. d) Shows a HAADF zoom-in of the interface along the perpendicular [11–20] ZA. Some bright contrasts that are believed to be related to inhomogeneous sulfur depletion and Cd enrichment. In e) the EDS mapping associated to d) shows slight diffusion of Zn in line with the with the S depletion observed in d).

and ZB segments can be recognized in the ZnS-WZ layer. The hexagonality yield was evaluated on different micrographs. For the sample grown at 520 °C (Fig. 7a and b), the ZnS-WZ layer includes numerous ZB segments underlined by colored red areas with the (0001) basal hexagonal planes parallel to the (111) cubic planes. It looks like the ZB segments are more present in the areas where tunnels are presents (encircled dark contrasts). Thus, the cavities related to thermal desorption look detrimental for the crystal quality of the epilayer. However, it is difficult to unequivocally associate the presence of ZB segments to a specific cavity as the cubic and hexagonal stacking are not discriminated along the ⟨0001⟩ ZA. The hexagonality yield can be estimated from these STEM micrographs by identifying the number of elementary cubic segments and calculating the length ratio of WZ zones with respect to the total analyzed length along the [0001] direction. From each image a hexagonality yield was extracted at the interface, resulting in an average of 75 % for the sample grown at 520 °C and around 91 % for samples grown at 360 °C. An uncertainty must be taken into account, which can be estimated to be approximately 2–3 %, depending on the quality of the image and our ability to identify the stacking. Indeed, the lowering of growth temperature enables to get rid of the formation of cavities and in turn improves the hexagonality yield in ZnS layers (Fig. 7). Besides, we note in Fig. 7b, that the hexagonality decreases with the increased thickness due to additional basal stacking faults (BSFs) nucleating randomly within the layer. This is not clearly understood and need to be further addressed.

Fig. 8 shows HAADF-STEM image and associated Fourier filtered image of line and planar defects formed in the ZnS-WZ layer of 545 nm thick from sample S6. The presence of extra half planes and associated edge dislocations originating at the ZnS/CdS interface, are evidenced by yellow symbols in the Fourier filtered image using a (0002) Bragg

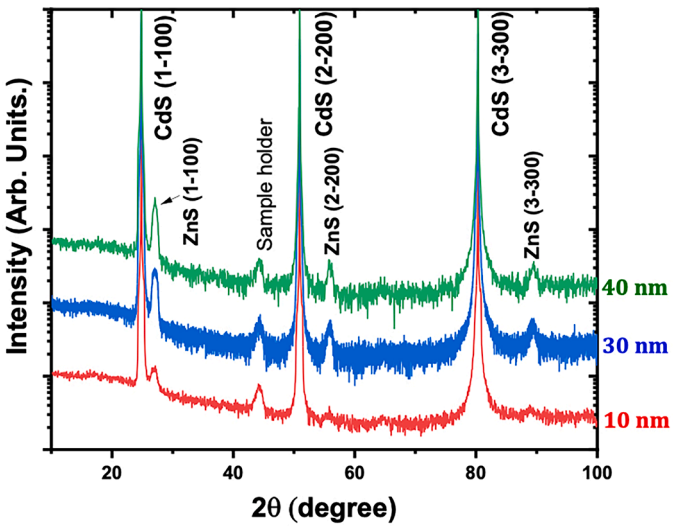


**Fig. 6.** XRD patterns for ω−2θ scans of samples S2 (40 nm), S3 (30 nm) and S5 (10 nm) grown at 360 °C.

reflection (Fig. 8a and e). These edge dislocations are considered as misfit dislocations with a burger vector of ½<0001>. They assist the relaxation of stress caused by lattice mismatch. The extra half planes are likely associated to planar defects such as stacking mismatch boundaries or inversion domain boundaries [65,66] that will require analyses of the polarity inversion at the boundary. Yet, the stacking sequence of the basal planes shows some basal stacking faults (BSFs) in the zones A, B C. As shown in zoom-in view in Fig. 8b-d, these BSFs are not exactly in line with the misfit dislocations. Their formation looks complex and could be supported by the formation of additional partial dislocations along ⟨1–100⟩ or ⟨2–1–10⟩. Although the stackings could correspond to extrinsic E and intrinsic $I_2$ BSFs, respectively with 3 and 2 cubic violations in the wurtzite stacking, the determination of the exact nature of the BSFs requires complete analyses by diffraction contrast TEM on plan views to identify the associated partial dislocations. Additionally, the Fourier filtered image with (−1101) reflection in Fig. 8f shows edge dislocations (symbols in blue) terminating planar defects on (−1101) planes that are likely connecting the BFSs. Such pyramidal defects are not often reported and require further investigation. Likewise, Fourier filtered image with (−1100) reflection in Fig. 8g shows several vacancy and interstitial prismatic loops on (−1100) planes evidenced respectively by face-to face red and green edge dislocation symbols.

On the other hand, prismatic faults on either {11–20} or {10–10} planes are often reported in hexagonal non-polar layers [67]. They should appear edge on if looked along [0001] zone axis. They are observed in ZnS-WZ layer, in Fig. 5b. The dark field micrograph, taken with a (11–20) Bragg reflection, shows that among threading dislocations straight bright contrast appear perpendicular to the m-plane surface therefore giving evidence of stacking faults on {11–20} planes.

## 4. Discussion

The microcrack formation arises from several factors related to the growth process, material properties or external stresses. Their formation in ZnS-WZ may result from a combination of TEC mismatch, cooling rate and stress anisotropy in the film. In WZ structures, the linear thermal expansion is anisotropic; it is larger along a-axis than along c-axis [68, 69]. For CdS-WZ, TEC at 300 K are respectively of $4.3 \times 10^{-6}$ $K^{-1}$ and $2.77 \times 10^{-6}$ $K^{-1}$ for a and c axes [68]. For ZnS-WZ, TEC were experimentally reported at $6.5 \times 10^{-6}$ $K^{-1}$ and $4.6 \times 10^{-6}$ $K^{-1}$ for a and c respectively [70] and were also calculated with density functional theory giving slightly larger values of $8.4 \times 10^{-6}$ $K^{-1}$ and $4.1 \times 10^{-6}$ $K^{-1}$ [69]. Thus, TEC mismatch and anisotropy may account for our observation of microcracks perpendicular to [11–20] direction (Fig. 3a and Fig. A5). However, other origin may not be disregarded. Mitigation solutions to this problem should be found such as careful control of the cooling rate to minimize thermal stresses and adjusting even lower deposition temperature to minimize thermal expansion.

Concerning the facets formed on the ZnS-WZ grown surface (Figs. 3a and 4a), no specific crystalline plane can be indexed. The hypothesis of a surface energy driving force can thus been ruled out. Similar sawtooth surface morphology was observed by Secco d'Aragona et al. [71] who suggest a connection with the formation of prismatic stacking faults. We indeed observe the presence of prismatic faults on {11–20} planes (Fig. 5b). Unfortunately, the large density of such stacking faults impedes to make a clear relation between the sawtooth surface morphology and the presence of prismatic fault as suggested.

It is important to note that this sawtooth morphology is associated to elongated structures along [0001] as are the grooves formed by thermal desorption of the CdS-WZ substrate. We believe that this feature could be accounted for complex anisotropic surface mechanisms. Basically, on m-plane, adatom interactions and surface diffusion should be different along a and c axes and may lead to different step edge energy. Such phenomenon has been observed and simulated for homoepitaxy of GaN on m-plane surfaces [72–74] resulting in elongated islands during

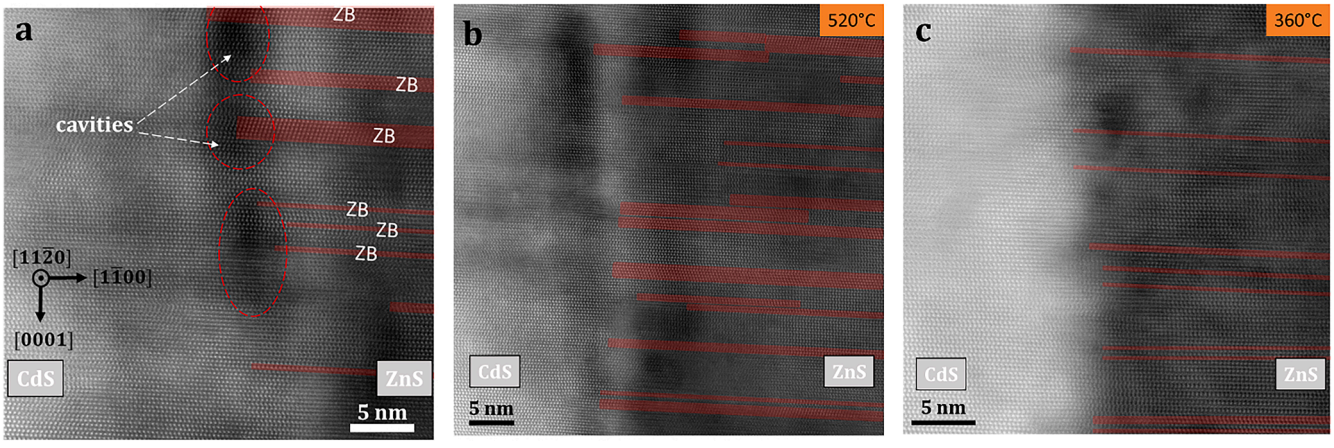


**Fig. 7.** HAADF HR-STEM micrographs of the CdS/ZnS interface along [11–20] ZA showing stackings faults forming cubic violations inserted in the hexagonal stacking of the ZnS-WZ layer. In a) for sample grown at 520 °C the presence of cavities under the interface is highlighted by dotted circles. In the cavity zone, ZB segments are present. The hexagonality yield is compared by underlining the cubic stacking and stacking faults in red for samples grown at 520 °C in b) and 360 °c in c) respectively.

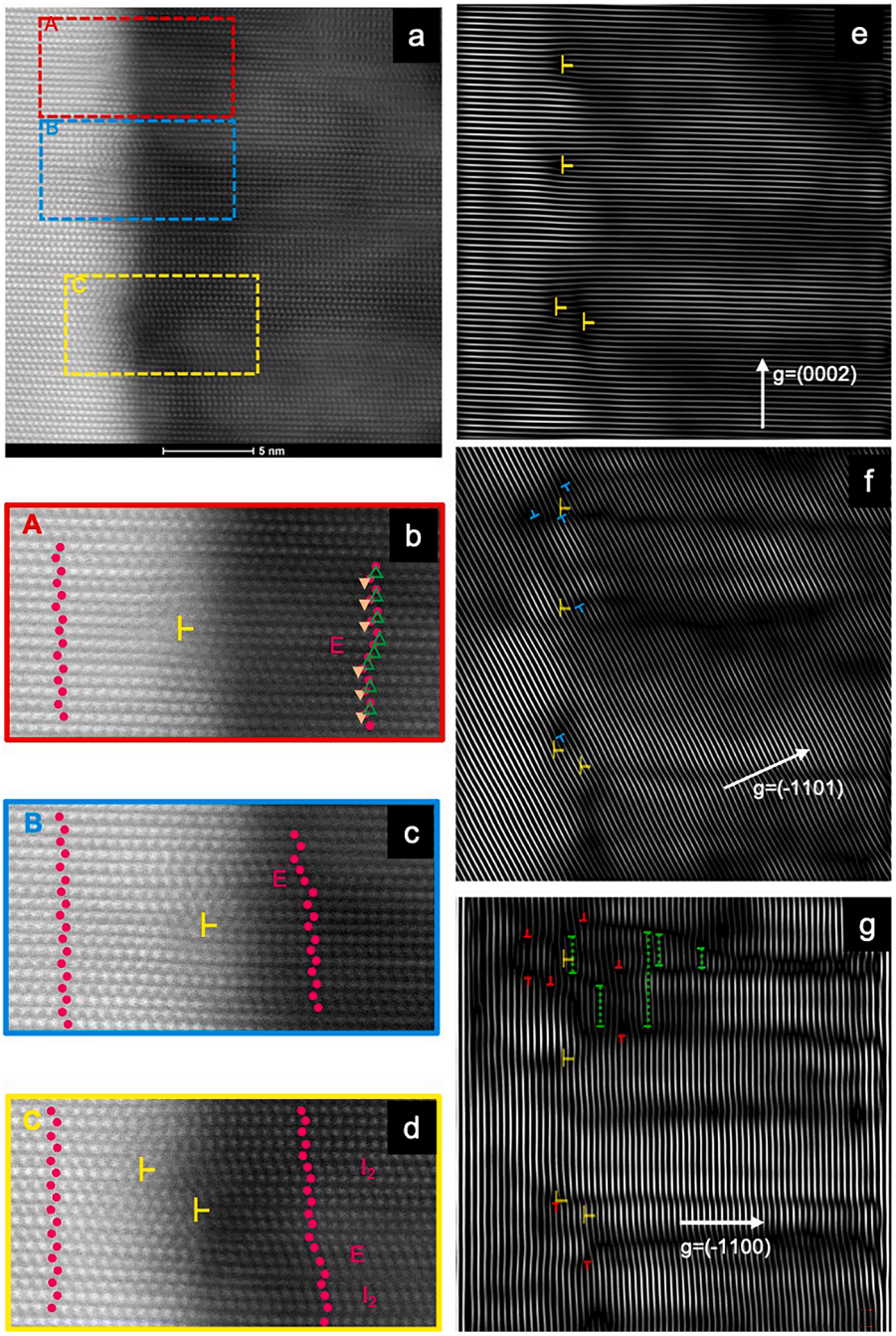


**Fig. 8.** a) HAADF STEM micrograph of the ZnS/CdS interface and the associated filtered Fourier images taken respectively with the (0002), (−1101) and (−1100) Bragg reflections (e, f and g). In e) yellow ⊥ symbols indicate edge dislocations on m-plane bounding an extra half basal planes. In f) Blue ⊥ symbols indicate edge dislocations with extra plane on (−1101) pyramidal planes. They look to be associated to the edge dislocations in e). In g) loops on prismatic planes are visible with a (−1100) reflection, respectively red for vacancy loops and green for interstitial loops. b,c and d) show high resolution zoom-in of zones A, B and C from a). They evidence the stacking sequences of basal planes that indicate different configurations of BSFs either extrinsic E or intrinsic $I_2$ based on the number of cubic violations.

growth. Molecular dynamic simulation would help in understanding those phenomena.

Up to now various approaches were explored to deposit ZnS-WZ films by MOCVD [35,75,76], as well as pulsed laser deposition (PLD) [77–79] and RF magnetron sputtering [80]. On the one hand, polycrystalline films were formed with the appearance of WZ phase depending on temperature and substrate [19,81–83]. Using PLD, Zhang et al. [78] obtained a good control of the WZ phase in polycrystalline films with a precise tuning of temperature of a Au-coated sapphire substrate. Xin et al. [79] claimed epitaxy of ZnS-WZ on (11–20) sapphire and (001) silicon using PLD but showed no diffraction pattern of TEM micrograph to support their claim. On the other hand, the epitaxial growth on single-crystal substrates such as Si, GaAs, GaP or (0001)-oriented sapphire only achieved zinc-blende structures [18,31,36,37]. In 1975, Lilley et al. [24] were the first to report a high temperature (>700 °C) growth of highly ordered hexagonal ZnS on non-polar (1–102) sapphire but without description of the structure. Then, Greenberg et al. [41] showed respectively that epitaxy on a-plane (11–20) and r- plane (10–12) -sapphire resulted in an oriented mixture of ZB and WZ with a strong preferred orientation relationship with the substrate. One must note that in that case the lattice mismatch is larger than 20 % for a-axis and 51 % for c-axis which make epitaxy difficult. By

adding an additional ZnO buffer layer to reduce lattice mismatch, Wang et al. [84] recently showed the possibility of an epitaxy of ZnS-WZ layer on a m-plane (1–100) ZnO/sapphire stacked substrate. However, they evidenced that the ZnS-WZ film was misoriented by 5.55° with respect to the underneath ZnO/Sapphire substrate probably. This could be explained by the compensation of lattice mismatch between ZnS and ZnO as well as the presence of lattice-mismatch defects in the ZnO buffer layer. In line with those findings, we show here that using a perfect CdS-WZ substrate with a reduced lattice mismatch with ZnS effectively enables the epitaxy of ZnS-WZ film without any misorientation with the substrate. On a backside, CdS is highly thermally instable, the lattice and TEC mismatches with ZnS are still too large and Cd is highly toxic. So that, alternative substrates would be preferable. However, there is no other single crystal material providing better lattice parameter matching with ZnS. One may suggest to use m-plane single ZnO substrates which have a TEC of $6.5 \times 10^{-6}$ $K^{-1}$ along a-axis and $3.7 \times 10^{-6}$ $K^{-1}$. But the lattice parameters along a-and c-axis are of 3.252 Å and 5.313 Å respectively giving a lattice mismatch of about 18 % and 33 %.

## 5. Conclusion

We show that the wurtzite structure can be achieved in ZnS thin films by forcing the stacking on non-polar surface. CdS substrate is used to provide a proof of concept of the epitaxy on m-plane surfaces although with disordered basal stacking faults due to the lattice mismatch between ZnS and CdS compounds. HR-STEM observations in cross section show misfit dislocations at the ZnS/CdS interface and basal stacking faults associated with pyramidal and prismatic stacking faults. XPS and AFM measurements demonstrate the efficiency of the proposed surface preparation process. However, a better suitable substrate should be found, i.e. better thermal stability and the lowest mismatch of lattice parameter and thermal expansion coefficient. ZnS-WZ may grow on other m-plane substrates providing the criteria of minimum lattice mismatch is fulfilled. This growth may be also applicable for metastable ZnSe-WZ on m-plane surfaces.

## CRediT authorship contribution statement

**Hassan Melhem:** Writing – original draft, Visualization, Investigation, Formal analysis, Data curation. **Geraldine Hallais:** Validation, Methodology, Investigation. **Gaelle Amiri:** Resources, Methodology, Investigation. **Gilles Patriarche:** Validation, Resources, Methodology, Investigation, Data curation. **Nathaniel Findling:** Investigation. **Theo Van den Berg:** Investigation. **Hafssa Ameziane:** Investigation. **Charles Renard:** Validation. **Vincent Sallet:** Validation, Supervision, Resources, Methodology, Investigation. **Laetitia Vincent:** Writing – review & editing, Writing – original draft, Visualization, Supervision, Project administration, Methodology, Investigation, Funding acquisition, Formal analysis, Conceptualization.

## Declaration of competing interest

The authors declare the following financial interests/personal relationships which may be considered as potential competing interests:

L. Vincent reports financial support was provided by European Commission. If there are other authors, they declare that they have no known competing financial interests or personal relationships that could have appeared to influence the work reported in this paper.

## Acknowledgments

This project received funding from the European Union's Horizon 2020 research and innovation program under grant agreement 964191 (OptoSilicon) and was supported by the French Renatech/Renatech+ networks. The project was parttially supported by the French Agence Nationale de la Recherche with the grants ANR-17-CE030-0014-01 and ANR-23-CE08-0020-01.

## Supplementary materials

Supplementary material associated with this article can be found, in the online version, at doi:10.1016/j.tsf.2025.140609.

## APPENDIX A

### *Surface preparation of the CdS substrates*

#### *XPS S2p core level spectrum*

The HR-XPS analysis in Fig. A1 performed on the S 2p on a CdS as-received sample reveals the presence of the characteristic doublet peaks, S 2p3/2 and S 2p1/2, respectively located at 161.4 eV and 162.5 eV. These peaks are indicative of metal sulfide bonds, specifically S-Cd, as previously reported in the literature. The decomposition of the spectrum confirms that no other components are bonded to sulfur, suggesting a pure metal sulfide phase. This consolidates our hypothesis of no sulfate formation on the surface.

#### *XPS spectrum of doublet peak of Br3p3/2 and Br3p1/2*

Fig. S2 shows the Br 3p core level doublet, Br 3p3/2 and Br 3p1/2, located at 182.1 eV and 188.9 eV, respectively, which reveals bromine contamination in the CdS sample after chemical mechanical polishing (CMP). The contamination has been estimated to be approximately 1.5 % across the entire surface. Our hypothesis is that this element is primarily bonded to Cd based on the results obtained for the Cd peak (see Fig. 1c in the main paper). However, since bromine is a very volatile element, we demonstrate that after annealing at 350 °C for 20 min, this contamination appears to be completely removed.

#### *RMS measurements*

The initial roughness was measured operating in tapping mode using a Veeco silicon tip on two CdS samples. The roughness was assessed by standard RMS (Root Mean Square) measurements and was around 0.46 ± 0.22 nm, along with the presence of scratches originating from the supplier. After CMP using 0.01 % bromine methanol ($Br_2$-MeOH) used to remove contamination for epitaxy surface preparation, we could reach a similar surface roughness to 0.40 ± 0.07 nm.

Table 2 in the main manuscript and Fig. A3 display the roughness measurements on a 16 $\mu m^2$ area performed before and after polishing, as well as after annealing at 360 and 520 °C under UHV for 10 min. It appears that surface roughness after annealing at 520 °C increases significantly, almost by a factor 2 compared to the reference surface. AFM image shows the presence of deep elongated grooves on the surface. The size and density of these grooves are likely to increase with increasing temperature or annealing duration. On the other hand, annealing at 360 °C showed no signs of groove formation, as evidenced by AFM measurements showing a barely unchanged roughness of 0.377 ± 0.035 nm for a CdS sample annealed at 360 °C under UHV.

Fig. A4 shows an AFM depth profile of a groove formed by thermal annealing during 10 min at 520 °C under hydrogen ($H_2$) and DTBS. The profile is acquired perpendicularly to the groove that is elongated along ⟨0001⟩ and exhibits a depression with a V-shape indicative of desorption during annealing. The width is around 40 nm and the depth about 4 nm. However, it looks like the convolution of the AFM tip with the groove sidewall does not enable an accurate value of the depth.

#### *Microcracks formation after ZnS deposition*

SEM image in Fig. A5 exhibits the surface morphology of the ZnS layer of the sample S2 and the formation of microcracks due to thermal expansion coefficient mismatch in between ZnS-WZ and CdS-WZ substrate. All the microcracks are elongated along the c-axis [0001]. This preferential orientation is likely related to the anisotropic thermal

expansion of both wurtzite materials. The intensity line-scan in Fig. A5b acquired perpendicularly to the microcracks indicate that they are almost periodically formed on the surface with period of around 0.8 μm.

*Crystallinity of the ZnS-WZ layer*

The Fig. A6 displays the Full Width at Half Maximum (FWHM) values of the (1–100) diffraction peak from the XRD pattern given in Fig. 6a. The FWHM values are relatively consistent for all the ZnS-WZ thicknesses, fluctuating slightly between 0.80° and 0.85°. this suggests a fairly good crystal quality of the layers that is not degraded by further thickening. These FWHM values around 0.80° can be explained by the presence of the dislocations and stacking faults described in Fig. 8.

## Data availability

Data will be made available on request.

## References


[1] J.S. McCloy, Properties and processing of chemical vapor deposited zinc sulfide, 2008, PhD Thesis of The University of Arizona, Publication Number: AAI3344627; ISBN: 9781109027716.
[2] E.V. Yashina, Preparation and properties of polycrystalline ZnS for IR applications, Inorg. Mater. 39 (7) (2003) 663–668.
[3] I.T. Steinberger, Polytypism in zinc sulphide, Prog. Cryst. Growth Char. 7 (1) (1983) 7–54.
[4] S. Mardix, Polytypism: a controlled thermodynamic phenomenon, Phys. Rev. B 33 (12) (1986) 8677–8684.
[5] S. G. Oleinik, V.D. Nina, Polytype formation in nonmetallic substances Russ. Chem. Rev. 66 (7) (1997) 553.
[6] C.-Y. Yeh, Z.W. Lu, S. Froyen, A. Zunger, Zinc-blende–wurtzite polytypism in semiconductors, Phys. Rev. B 46 (16) (1992) 10086–10097.
[7] T. Ito, Simple criterion for wurtzite-zinc-blende polytypism in semiconductors, Jpn. J. Appl. Phys. 37 (10B) (1998) L1217.
[8] T. Ito, T. Kondo, T. Akiyama, K. Nakamura, Theoretical investigations for the polytypism in semiconductors, J. Cryst. Growth 318 (1) (2011) 141–144.
[9] F. Boutaiba, A. Belabbes, M. Ferhat, F. Bechstedt, Polytypism in ZnS, ZnSe, and ZnTe: first-principles study, Phys. Rev. B 89 (24) (2014) 245308.
[10] E.T. Allen, J.L. Crenshaw, H.E. Merwin, The sulphides of zinc, cadmium and mercury: their crystalline forms and genetic conditions, Am. J. Sci. XXXIV (1912).
[11] V.G. Hill, Phase transformation in zinc sulphide, Can. Mineral. 6 (2) (1958) 234–259.
[12] J. Baars, G. Brandt, Structural phase transitions in ZnS, J. Phys. Chem. Solids 34 (5) (1973) 905–909.
[13] M. Akizuki, Slip structure of heated sphalerite, Am. Mineral. 55 (7–8) (1970) 1302–1312.
[14] E. Lendvay, Growth of structurally pure cubic and hexagonal ZnS single crystals, J. Cryst. Growth 10 (1) (1971) 77–84.
[15] P. Wu, R. Kershaw, K. Dwight, A. Wold, Growth and characterization of nickel-doped ZnS single crystals, Mater. Res. Bull. 24 (1) (1989) 49–53.
[16] W.M. Yim, E.J. Stofko, Vapor-phase epitaxial growth and some properties of ZnSe, ZnS, and CdS, J. Electrochem. Soc. 119 (3) (1972) 381.
[17] J.B. Mullin, S.J.C. Irvine, J. Giess, A. Royle, Recent developments in the MOVPE of II–VI compounds, J. Cryst. Growth 72 (1) (1985) 1–12.
[18] N.H. Tran, A.J. Hartmann, R.N. Lamb, Epitaxial ZnS thin films grown by single source chemical vapor deposition, J. Phys. Chem. B 104 (6) (2000) 1150–1152.
[19] Y.-G. Yoon, I.-H. Choi, Preparation of ZnS thin films by using photoassisted MOCVD, J. Korean Phys. Soc. 63 (8) (2013) 1609–1614.
[20] P.J. Wright, B. Cockayne, A.J. Williams, MOVPE growth of CdxZn1-xS, J. Cryst. Growth 72 (1) (1985) 23–26.
[21] B. Cockyane, P.J. Wright, Metalorganic chemical vapour deposition of wide band gap II–VI compounds, J. Cryst. Growth 68 (1) (1984) 223–230.
[22] T. Imai, S. Fuke, H. Araki, K. Kuwahara, Dependence of substrate materials on the growth of ZnS on GaAs and GaP substrates, J. Cryst. Growth 94 (4) (1989) 983–986.
[23] C. Thiandoume, O. Ka, A. Lusson, O. Gorochov, MOVPE growth of ZnS on (100) GaAs using dimethylzinc and ditertiarybutyl sulphide precursors, J. Cryst. Growth 197 (4) (1999) 805–810.
[24] P. Lilley, P.M.R. Kay, C.N.W. Litting, The vapour phase deposition of thick epitaxial (100) ZnS layers on elemental and compound substrates in H2 gas flow, J. Mater. Sci. 10 (8) (1975) 1317–1322.
[25] V. Sallet, A. Lusson, M. Rommeluere, O. Gorochov, MOCVD growth and characterization of ZnS and Zn1−xMgxS alloys, J. Cryst. Growth 220 (2000) 209–215.
[26] K. Ichino, T. Onishi, Y. Kawakami, S. Fujita, S. Fujita, Growth of ZnS and ZnCdSSe alloys on GaP using an elemental sulfur source by molecular beam epitaxy, J. Cryst. Growth 138 (1) (1994) 28–34.
[27] K. Ichino, K. Ueyama, M. Yamamoto, H. Kariya, H. Miyata, H. Misasa, M. Kitagawa, H. Kobayashi, High temperature growth of ZnS and ZnMgS by molecular beam epitaxy under high sulfur beam pressure, J. Appl. Phys. 87 (9) (2000) 4249–4253.
[28] M. Yokoyama, K.-i. Kashiro, S.-i. Ohta, Molecular beam epitaxial growth of ZnS on a (100)-oriented Si substrate, J. Cryst. Growth 81 (1) (1987) 73–78.
[29] S. Kaneda, S. Satou, T. Setoyama, S.-i. Motoyama, M. Yokoyama, N. Ota, Single crystal growth of ZnS by the method of gas source MBE, J. Cryst. Growth 76 (2) (1986) 440–448.
[30] H. Kanie, H. Araki, K. Ishizaka, H. Ohta, S. Murakami, Epitaxial growth of ZnS on GaP by molecular beam deposition, J. Cryst. Growth 138 (1) (1994) 145–149.
[31] S.A. Telfer, C. Morhain, B. Urbaszek, C. O'Donnell, P. Tomasini, A. Balocchi, K. A. Prior, B.C. Cavenett, MBE growth of ZnS and ZnCdS layers on GaP, J. Cryst. Growth 214-215 (2000) 197–201.
[32] W. Tong, B.K. Wagner, T.K. Tran, W. Ogle, W. Park, C.J. Summers, Kinetics of chemical beam epitaxy for high quality ZnS film growth, J. Cryst. Growth 164 (1) (1996) 202–207.
[33] J.W. Cook Jr., D.B. Eason, R.P. Vaudo, J.F. Schetzina, Molecular-beam epitaxy of ZnS using an elemental S source, J. Vac. Sci. Technol. B: Microelectronics and Nanometer Structures Processing, Measurement, and Phenomena 10 (2) (1992) 901–904.
[34] S. Kaneda, T. Shimoguchi, H. Takahashi, S.i. Motoyama, F. Kano, M. Yokoyama, S. Satou, Optimum growth condition of single-crystalline undoped ZnS grown by the molecular-beam-epitaxial method using a H2S gas source, J. Appl. Phys. 64 (8) (1988) 3945–3948.
[35] V. Miikkulainen, M. Leskelä, M. Ritala, R. Puurunen, ChemInform Abstract, Crystallinity of inorganic films grown by atomic layer deposition: overview and general trends, J. Appl. Phys. 113 (2013).
[36] T. Tadokoro, S.-i. Ohta, T. Ishiguro, Y. Ichinose, S. Kobayashi, N. Yamamoto, Atomic layer epitaxy growth of ZnS on (100)GaAs using molecular beam epitaxy system, J. Cryst. Growth 148 (3) (1995) 223–231.
[37] J.W. McCamy, D.H. Lowndes, J.D. Budai, R.A. Zuhr, X. Zhang, Epitaxial ZnS films grown on GaAs (001) and (111) by pulsed-laser ablation, J. Appl. Phys. 73 (11) (1993) 7818–7822.
[38] H. Hiramatsu, H. Ohta, M. Hirano, H. Hosono, Heteroepitaxial growth of single-phase zinc blende ZnS films on transparent substrates by pulsed laser deposition under H2S atmosphere, Solid. State Commun. 124 (10) (2002) 411–415.
[39] H. Okumura, S. Misawa, S. Yoshida, Epitaxial growth of cubic and hexagonal GaN on GaAs by gas-source molecular-beam epitaxy, Appl. Phys. Lett. 59 (9) (1991) 1058–1060.
[40] H. Okumura, K. Ohta, G. Feuillet, K. Balakrishnan, S. Chichibu, H. Hamaguchi, P. Hacke, S. Yoshida, Growth and characterization of cubic GaN, J. Cryst. Growth 178 (1) (1997) 113–133.
[41] B. Greenberg, W.K. Zwicker, I. Cadoff, ZnS epitaxy on sapphire {110}, Thin. Solid. Films. 141 (1) (1986) 89–97.
[42] K. Okita, K. Inaba, Z. Yatabe, Y. Nakamura, Structural characteristics of a non-polar ZnS layer on a ZnO buffer layer formed on a sapphire substrate by mist chemical vapor deposition, Jpn. J. Appl. Phys. 57 (6) (2018) 065503.
[43] H.F. McMurdie, M.C. Morris, E.H. Evans, B. Paretzkin, W. Wong-Ng, L. Ettlinger, C. R. Hubbard, Standard X-ray diffraction powder patterns from the JCPDS Research Associateship, Powder. Diffr. 1 (2) (1986) 64–77.
[44] N.A. Razik, Use of a standard reference material for precise lattice parameter determination of materials of hexagonal crystal structure, J. Mater. Sci. Lett. 6 (12) (1987) 1443–1444.
[45] S.H. Shah, A. Azam, M.A. Rafiq, Atomistic simulations of CdS morphologies, Cryst. Growth Des. 15 (4) (2015) 1792–1800.
[46] S.H. Na, C.H. Park, First-principles study of the surface of wurtzite ZnO and ZnS - implications for nanostructure formation, J. Korean Phys. Soc. 54 (2009) 867–872.
[47] S. Kumar, F. Fossard, G. Amiri, J.-M. Chauveau, V. Sallet, MOCVD growth and structural properties of ZnS nanowires: a case study of polytypism, Nanomaterials 12 (14) (2022) 2323.
[48] C. Thiandoume, V. Sallet, R. Triboulet, O. Gorochov, Decomposition kinetics of tertiarybutanol and diethylzinc used as precursor sources for the growth of ZnO, J. Cryst. Growth 311 (5) (2009) 1411–1415.
[49] H. Dumont, A. Marbeuf, J.E. Bourée, O. Gorochov, Mass-spectrometric study of thermal decomposition of diethylzinc and diethyltellurium, J. Mater. Chem. 2 (9) (1992) 923–930.
[50] G. Martin, N. Barroeta, Gas phase thermolysis of sulfur compounds. II. Ditertiary butyl sulfide, Int. J. Chem. Kinet. 12 (10) (1980) 699–716.
[51] E.I. Givargizov, P.A. Babasian, Vaporization mechanism and kinetics of AIIBVI compounds, J. Cryst. Growth 37 (2) (1977) 129–139.
[52] G. Beamson, D.R. Briggs, High resolution XPS of organic polymers: the Scienta ESCA300 database, 1992.
[53] M.C. Ortega-Liebana, N.X. Chung, R. Limpens, L. Gomez, J.L. Hueso, J. Santamaria, T. Gregorkiewicz, Uniform luminescent carbon nanodots prepared by rapid pyrolysis of organic precursors confined within nanoporous templating structures, Carbon. N. Y. 117 (2017) 437–446.
[54] https://srdata.nist.gov/xps/EnergyTypeElement. 2023. accessed May, 2024, version 5.0.
[55] M. Marychurch, G.C. Morris, X-ray photoelectron spectra of crystal and thin film cadmium sulphide, Surf. Sci. Lett. 154 (2) (1985) L251–L254.
[56] V.G. Bhide, S. Salkalachen, A.C. Rastog, C.N.R. Rao, M.S. Hegde, Depth profile composition studies of thin film CdS:cu2S solar cells using XPS and AES, J. Phys. D. Appl. Phys. 14 (9) (1981) 1647.
[57] J.A. Bragagnolo, K.W. Böer, C. Wright, Thermally stimulated desorption from class I CdS crystals and its effect on their electrical properties, Phys. Status Solidi(A) 24 (1) (1974) 147–158.

[58] Z.A. Munir, J.P. Hirth, Surface morphology of sublimated crystals of cadmium and zinc sulfides, J. Appl. Phys. 41 (6) (1970) 2697–2704.
[59] G.A. Somorjai, N.R. Stemple, Orientation dependence of the evaporation rate of CdS single crystals, J. Appl. Phys. 35 (11) (1964) 3398–3400.
[60] B. Krishnan, S. Shaji, M. Acosta-Enriquez, E. Acosta-Enriquez, R. Ortega, M. Zayas, S. Castillo, I. Palamà, E. D'Amone, M.I. Pech-Canul, S. D'Amone, B. Cortese, Group II–VI Semiconductors, in Semiconductors: Synthesis, Properties and Applications, M. I. Pech-Canul and N. M. Ravindra, eds. Springer International Publishing (2019) pp. 397–464.
[61] R.A. Babasian, E.I. Givargizov, Vaporization of CdS single crystals and formation of negative whiskers, J. Mater. Sci. 15 (7) (1980) 1619–1624.
[62] F. Seker, K. Meeker, T.F. Kuech, A.B. Ellis, Surface chemistry of prototypical bulk II−VI and III−V semiconductors and implications for chemical sensing, Chem. Rev. 100 (7) (2000) 2505–2536.
[63] W.H. Strehlow, Chemical polishing of II-VI compounds, J. Appl. Phys. 40 (7) (1969) 2928–2932.
[64] R.D. Seals, R. Alexander, L.T. Taylor, J.G. Dillard, Core electron binding energy study of group IIb-VIIa compounds, Inorg. Chem. 12 (10) (1973) 2485–2487.
[65] C. Mauder, Physics, MOVPE growth and investigation of m-plane GaN films and InGaN/GaN quantum wells on γ-LiAlO2 substrates, 2011, PhD thesis of Technische Hochschule Aachen (Germany). Fakultaet fuer Elektrotechnik und Informationstechnik, reference number 44026075.
[66] J.E. Northrup, J. Neugebauer, L.T. Romano, Inversion domain and stacking mismatch boundaries in GaN, Phys. Rev. Lett. 77 (1) (1996) 103–106.
[67] W. Neumann, A. Mogilatenko, T. Wernicke, E. Richter, M. Weyers, M. Kneissl, Structure investigations of nonpolar GaN layers, J. Microsc. 237 (3) (2010) 308–313.
[68] H. Iwanaga, A. Kunishige, S. Takeuchi, Anisotropic thermal expansion in wurtzite-type crystals, J. Mater. Sci. 35 (10) (2000) 2451–2454.
[69] S.Q. Wang, First-principles study of the anisotropic thermal expansion of wurtzite ZnS, Appl. Phys. Lett. 88 (6) (2006).
[70] R.R. Reeber, G.W. Powell, Thermal expansion of ZnS from 2° to 317°K, J. Appl. Phys. 38 (4) (1967) 1531–1534.
[71] F. SECCO D'ARAGONA, P. DELAVIGNETTE, Fautes de croissance dans LA wurtzite, J. Phys. Colloques 27 (C3) (1966) C3. -121-C3-127In French.
[72] E. Perret, D. Xu, M.J. Highland, G.B. Stephenson, P. Zapol, P.H. Fuoss, A. Munkholm, C. Thompson, Island dynamics and anisotropy during vapor phase epitaxy of m-plane GaN, Appl. Phys. Lett. 111 (23) (2017) 232102.
[73] D. Xu, P. Zapol, G.B. Stephenson, C. Thompson, Kinetic Monte Carlo simulations of GaN homoepitaxy on c- and m-plane surfaces, J. Chem. Phys. 146 (14) (2017) 144702.
[74] L. Lymperakis, J. Neugebauer, Large anisotropic adatom kinetics on nonpolar GaN surfaces: consequences for surface morphologies and nanowire growth, Phys. Rev. B 79 (24) (2009) 241308.
[75] S. Takata, T. Minami, T. Miyata, H. Nanto, Growth of hexagonal ZnS thin films by MOCVD using CS2 gas as a sulfur source, J. Cryst. Growth 86 (1) (1988) 257–262.
[76] P.B. Smith, Preparation and characterization of ZnS thin films produced by metalorganic chemical vapor deposition, J. Vac. Sci. Technol. A 7 (3) (1989) 1451–1455.
[77] R.B. Ettlinger, A. Cazzaniga, S. Canulescu, N. Pryds, J. Schou, Pulsed laser deposition from ZnS and Cu2SnS3 multicomponent targets, Appl. Surf. Sci. 336 (2015) 385–390.
[78] W. Zhang, X. Zeng, J. Lu, H. Chen, Phase controlled synthesis and optical properties of ZnS thin films by pulsed laser deposition, Mater. Res. Bull. 48 (10) (2013) 3843–3846.
[79] Z.-J. Xin, R. Peaty, H. Rutt, R. Eason, Epitaxial growth of high-quality ZnS films on sapphire and silicon by pulsed laser deposition, Semicond. Sci. Technol. 14 (1999).
[80] J. Díaz-Reyes, R.S. Castillo-Ojeda, R. Sánchez-Espíndola, M. Galván-Arellano, O. Zaca-Morán, Structural and optical characterization of wurtzite type ZnS, Curr. Appl. Phys. 15 (2) (2015) 103–109.
[81] J. Fang, P.H. Holloway, J.E. Yu, K.S. Jones, B. Pathangey, E. Brettschneider, T. J. Anderson, MOCVD growth of non-epitaxial and epitaxial ZnS thin films, Appl. Surf. Sci. 70-71 (1993) 701–706.
[82] Y.S. Kim, S.J. Yun, Studies on polycrystalline ZnS thin films grown by atomic layer deposition for electroluminescent applications, Appl. Surf. Sci. 229 (1) (2004) 105–111.
[83] J.A. Lahtinen, A. Lu, T. Tuomi, M. Tammenmaa, Effect of growth temperature on the electronic energy band and crystal structure of ZnS thin films grown using atomic layer epitaxy, J. Appl. Phys. 58 (5) (1985) 1851–1853.
[84] L. Wang, K. Xiong, Y. He, X. Huang, J. Xia, X. Li, Y. Gu, H. Cheng, X. Meng, Epitaxial growth of wafer-scale two-dimensional polytypic ZnS thin films on ZnO substrates, CrystEngComm. 19 (17) (2017) 2294–2299.